Nano Energy 109 (2023) 108282

Contents lists available at ScienceDirect

Nano Energy

journal homepage: www.elsevier.com/locate/nanoen

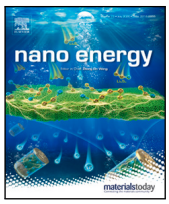

Full paper

# Self-powered triboelectric MEMS accelerometer

Mohammad Alzgool [a], Yu Tian [a], Benyamin Davaji [b], Shahrzad Towfighian [a,*]

[a] Binghamton University, 4400 Vestal Parkway East, Binghamton, NY 13902, United States of America
[b] Northeastern University, 360 Huntington Ave, Boston, MA 02115, United States of America

ARTICLE INFO

*Keywords:*
Tribo-electric-nano-generator (TENG)
MEMS
Accelerometer
Self-powered
Polyimide

ABSTRACT

A self-powered triboelectric accelerometer miniaturized to the micro-scale is presented. This micro triboelectric accelerometer (MTEA) was fabricated using CMOS-compatible processes. The design followed the triboelectric nanogenerators made in meso-scale and operates in the contact-separation mode. The scaled-down, multilayer design enabled fabrication using microelectromechanical systems (MEMS) technology. The MTEA was made using an aluminum and polyimide triboelectric pair that generated charges on the contact. A square movable plate that is 2 mm × 2 mm was fabricated with 1 μm thickness. Then, the fabricated MTEA was excited by a mini-shaker at known frequencies (0.1–7 kHz) and accelerations (1–10 g), and the output was recorded. The output was 0.7 V at the resonance frequency (700 Hz). The generated voltage has a linear relationship with the acceleration with a maximum sensitivity of 70 mV/g at the 700 Hz excitation frequency.

## 1. Introduction

Microelectromechanical systems (MEMS) are widely designed and integrated into various sensors and actuators in multiple fields of industry and science. As one of the most critical sensing applications, MEMS accelerometers can measure the dynamic acceleration forces acting on a proof mass by converting the mechanical movement into an electrical signal as an output. Sensitive accelerometers are necessary for many applications in the automotive industry [1,2], smart electronics [3–5], shipment monitoring [6,7], fitness tracking [8,9], etc.

Among the MEMS accelerometers developed in the past few years, capacitive electrostatic accelerometers are the most popular as they are compatible with nanofabrication techniques needed to integrate with numerous electronic components. In nicely designed electrostatic MEMS accelerometers [10–13], measurements of the displacements of the proof mass from the acceleration forces are directly related to variation in capacitance in an externally charged pair of parallel electrodes [14–16]. To mitigate the pull-in instability in the parallel plate designs, Daechin et al. built electrostatic-levitation-based MEMS accelerometers using multiple electrodes [13,17]. This strategy permitted devices with tunable natural frequencies, which allowed the measurement of acceleration in a much wider frequency range compared with conventional electrostatic MEMS accelerometers. Also, measuring the acceleration of the suspended electrode when it is levitated away from the bottom electrode has been proven effective in electromagnetic MEMS accelerometers. Because the electromagnetic suspension system has less friction and dynamic characteristics that are tunable by adjusting the circuits, electromagnetic MEMS accelerometers can achieve very high sensitivity, and accuracy [18], albeit rather high power consumption is unavoidable. Optical accelerometers have been investigated recently because of their very high-resolution sensitivity. Acceleration drives the proof mass and results in shifts of the resonant frequency [19], wavelengths [20], etc. These devices have to be fabricated precisely to incorporate delicate optical elements and are suitable for measuring accelerations in the high-frequency range of MHz. Tunneling accelerometers take advantage of the concept of tunneling currents. When the acceleration is applied, the distance between a tunneling tip and the counter electrode changes accordingly, which generates currents of different levels. Feedback circuits are built to keep the current or the distance constant by external forces [21].

Because capacitive MEMS accelerometers require external bias voltages for charging and electromagnetic MEMS accelerometers require large currents, neither is considered self-powered [22]. With the MEMS accelerometers designed to communicate with diverse components and integrate into devices with complex functionality, many researchers have been attempting to limit energy consumption to secure better reliability in sensors [23,24]. Piezoelectric materials are well-known to self-generate a potential difference following the strains in the structures. Many zero-power piezoelectric MEMS sensors [25,26] and digital triggers [27,28] for switches have been developed. Because no external energy sources and complicated amplifying electronics

* Corresponding author.
*E-mail addresses:* malzgoo1@binghamton.edu (M. Alzgool), ytian30@binghamton.edu (Y. Tian), b.davaji@northeastern.edu (B. Davaji), stowfigh@binghamton.edu (S. Towfighian).

https://doi.org/10.1016/j.nanoen.2023.108282
Received 11 December 2022; Received in revised form 8 February 2023; Accepted 11 February 2023
Available online 16 February 2023

are applied, piezoelectric MEMS sensors are regarded as self-powered. Investigations on piezoelectric MEMS accelerometers have been done for decades, with many effective designs developed [27,29]. The primary disadvantages of piezoelectric MEMS accelerometers are related to fabrication; the piezoelectric thin film often requires additional polarization after annealing to ensure a good sensitivity [30,31]. Even if the thin-film deposition is successful, the piezoelectric coupling between applied forces and electrical outputs is vastly reduced [32,33]. Therefore, their sensing performances and the potential to integrate with diverse electrical components are very limited.

In 2012, an innovative design of a flexible triboelectric nanogenerator (TENG) was demonstrated by Fengru et al. which takes advantage of the charge induced in the frictional contact and separation of two materials with distinct electron affinity [34]. Besides the effectiveness in transferring mechanical energy to electrical signals, TENG shows the advantages of low cost in fabrication, large power outputs, robust mechanical structures, and compatibility with diverse electronics [35–38]. Thus, many studies have been devoted to designing TENG-driven actuators such as a high-speed micro motor by Yang et al. [39] and self-powered TENG-based sensors by applying triboelectric pairs to various scenarios and utilizing or measuring the output voltages directly from the triboelectric effect [40–42]. In the realization of self-powered TENG-based accelerometers [43–45], the devices are conventionally in mesa-scale (cm × cm) and essentially work at low vibration frequencies. Considering the development of the internet of things (IoT) and various microsystems, there is a need to create microscale self-powered accelerometers with a high sensitivity. Through decades of process development for manufacturing MEMS devices, CMOS-compatible techniques such as plasma-enhanced chemical vapor deposition (PECVD) and deep reactive ion etching (DeepRIE) have become mature technologies and are widely used for high-volume production. Chen et al. [46] presented a micro triboelectric acoustic harvester fabricated from MEMS technologies. The merger of MEMS and TENG is promising to miniaturize the TENG and improve the integration of a self-powered sensing system into a microchip. However, the fabrication processes, including wafer bonding, still need to be simplified to facilitate inexpensive mass production. The latest work by Hamid et al. [42] used the MEMS processes and UV-LIGA (in German: ultra-Violet Lithographie, Galvanoformung, Abformung) as a novel hybrid technique to effortlessly form the proof mass in a TENG-based energy harvester. That work shows great potential to fabricate self-powered TENG-based devices on a micro-scale. However, the UV-LIGA process is not compatible with the MEMS standard microfabrication processes and its use of X-ray adds potential hazard to human beings [47–49].

In this work, we exhibit a TENG-based self-powered MEMS accelerometer fabricated only in the standard MEMS processes. The accelerometer outputs the directly generated voltage following the exerting acceleration force, and at the same time, no external voltage inputs are required. Mass production of the MEMS device is possible. Its high sensitivity and linear relationship mean it is competitive in various acceleration measurement scenarios.

## 2. Design and fabrication

The micro triboelectric accelerometer (MTEA) was fabricated with a bottom electrode of aluminum covered with polyimide on top, a gap, and a top electrode made of aluminum and an amorphous-silicon (a-Si) proof mass. To accomplish the fabrication, we designed 7 lithography masks to fabricate the MTEA layers. A schematic of the fabrication process is shown in Fig. 1. The fabrication process began with a 100 mm silicon wafer covered with an insulating layer of reactive-sputtered aluminum nitride (1.7 μm). Then, a 200 nm film of chrome and aluminum was sputtered to create the bottom layer (Cr/Al). The resulting film was patterned using Mask1 and an Inductive Conductive Plasma Reactive Ion Etcher (ICP-RIE) in $BCl_3$, $Cl_2$, and argon etch chemistry (Fig. 1a).

**Table 1**
TENG-based accelerometer dimensions.

| Description | Symbol | Value |
|---|---|---|
| Bottom electrode thickness | $t_b$ | 200 nm |
| Polyimide thickness | $t_p$ | 5 μm |
| Gap | $g$ | 2 μm |
| Top electrode thickness | $t_T$ | 120 nm |
| Proof mass thickness | $t_{pm}$ | 1 μm |
| Top electrode area | $A$ | 4 $mm^2$ |
| Square array elevation | $t_s$ | 1 μm |

Then, a 5 μm polyimide (PI2574 HD Microsystems) precursor was coated and baked until it was fully cured in a polyimide oven. The cured polyimide was then patterned using Mask2 and a reactive ion etching machine (RIE) with a $CF_4/O_2$ mixture that was tested for polyimide etching by Turban et al. [50] (Fig. 1b).

After the polyimide was patterned, a layer of 2 μm silicon oxide was deposited using plasma-enhanced physical vapor deposition (PECVD). The oxide film was patterned using Mask3 and RIE machine with $CHF_3$ and argon gases (Fig. 1c). While this mask was used to etch 2 μm of the oxide, a recipe of $CHF_3$ and $O_2$ was used to etch 1 μm of oxide with Mask4 which is made of a square pattern to create an arrayed structure in the top layer (Fig. 1d). That arrayed pattern increases the friction between the top aluminum layer and the bottom polyimide because of the increased surface area for aluminum in contact with the polyimide and, in return, will increase the surface charges when both layers collide. Then, a 120 nm Cr/Al-s film was deposited on top of the oxide. The film will conformally cover the square trenches created by the etching performed with Mask4. This film was etched using Mask5, and an ICP-RIE etcher was used to pattern the springs and the shape of the top electrode (Fig. 1e).

The top Cr/Al-s film has a compressive stress which if released will cause the electrode to collapse. To avoid that, a layer with tensile stress should be added to counter the compressive stress. In this design, we choose amorphous silicon to serve as the proof mass layer. Amorphous silicon deposited with PECVD has controllable stress that can be tuned by varying deposition pressure, temperature, and plasma power. We found that under a temperature of 200 °C, RF power of 20 W, and pressure of 2 torr, the Cr/Al and amorphous silicon film combination has a tensile stress of around 100 MPa or less. A 1 μm PECVD film of amorphous silicon was deposited on the patterned Cr/Al-s film. Because amorphous silicon is an insulating layer, it was etched from the top of the contact pads using Mask6, then both amorphous silicon and Cr/Al-s layers were etched to create the top electrode with release holes using Mask7 (Fig. 1f). The amorphous silicon etching was done using an RIE etcher with $SF_6/O_2$ gases, and the aluminum was etched using the same recipe as in Fig. 1a.

Finally, the wafer was diced and the vapor hydrofluoric (vHF) acid was used to remove the silicon oxide release layer and the release the top layer. This process takes 90–120 min. The released devices are wire-bonded using aluminum wires. A 3D schematic of the fabricated device is shown in Fig. 2a, and a microscopic image of the fabricated device is shown in Fig. 2b. The dimensions of the device are listed in Table 1. The fabrication process used for the accelerometer has many advantages over previous work were the triboelectric generator was made with UV-LIGA technology [42]. By using polyimide (PI2574), the deposition of 5 μm layer is easier as compared to the deposition of teflon since it can be done by spin-coating and oven-baking once to get the required thickness, and because the used polyimide precursor does not require adhesion promoter. The other major advantage of this work is the use of silicon dioxide as a sacrificial layer instead of polyimide (HD 4400). The silicon dioxide layer can be removed by vHF process relatively fast (typically around 2 h) compared to the process of removing the polyimide sacrificial layer as it was reported that ashing process under high-pressure oxygen was used for 800 h to remove 14 μm thick polyimide.

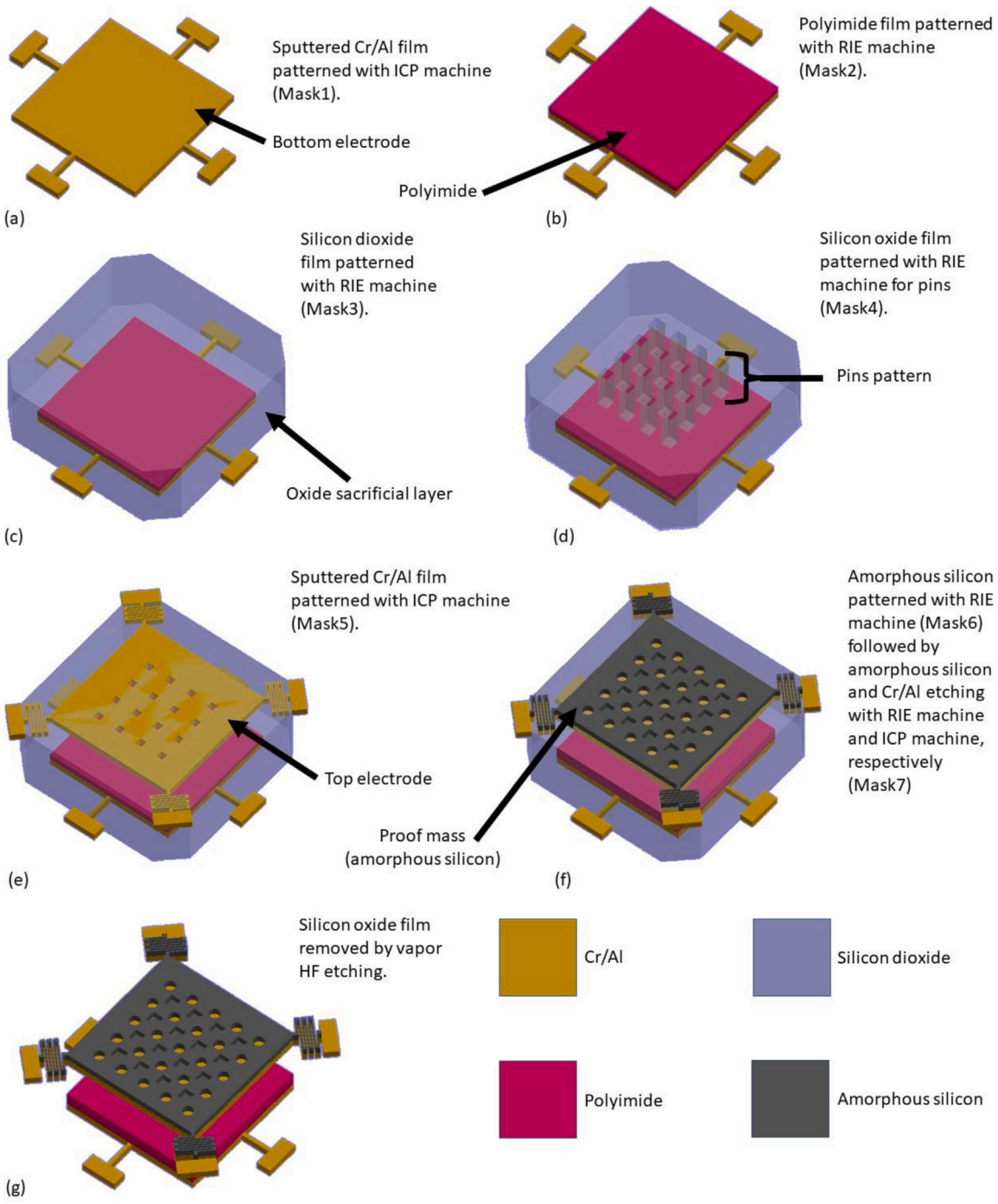


**Fig. 1.** CMOS fabrication process of the micro triboelectric accelerometer (MTEA).

## 3. Modeling and simulation

The model of the micro triboelectric accelerometer can be fundamentally simplified as in Fig. 2c; the micro plate and the serpentine springs attached to the amorphous silicon provide the proof mass and the necessary stiffness in vibration. At the same time, Cr/Al layers work as the top and bottom electrodes, and the polyimide layer is used to generate a charge when contacting the top electrode. We follow the derivations discussed in [51] to establish the electro-mechanical equations to predict the response of the accelerometer.

After the triboelectric pair is forced to contact, as a result of electrification, static charges of opposite signs and equal charge density $\sigma$ will be uniformly distributed on the surfaces of the top electrode and the polyimide layer with almost no decay. When the triboelectric pair separates, the induced potential difference will help transfer some amount of the charges, $q(t)$, between the top electrode and the bottom electrode. Considering the effect of static charge density $\sigma$ and transferred charges $q(t)$, there are generated electrical fields in the air gap and inside the polyimide layer. The strengths of the electric fields are derived ($E_a$: air, $E_p$: polyimide) as

$$E_a(t) = \frac{-q(t)/A + \sigma}{\epsilon_0}$$
$$E_p(t) = \frac{-q(t)/A}{\epsilon_0 \epsilon_r} \quad (1)$$

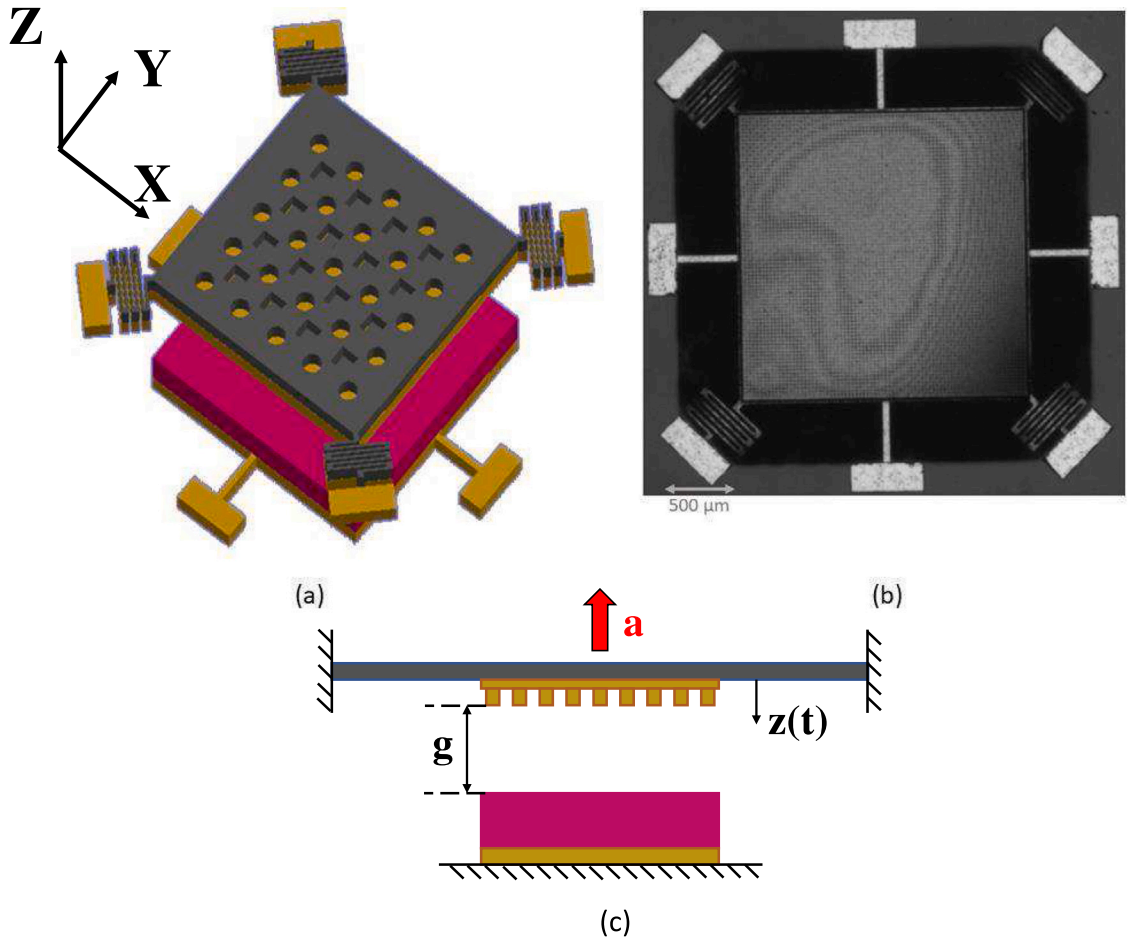


**Fig. 2.** (a) MTEA 3D schematic layout, (b) microscopic image of the MTEA, (c) schematic for the MTEA model.

where $A$ represents the total area of the micro plate, $\epsilon_0$ and $\epsilon_r$ are the vacuum permittivity and dielectric constant of the polyimide, respectively.

The produced voltage between the two electrodes can be written as

$$V(t) = E_a(t)\cdot\left(g - z(t)\right) + E_p(t)\cdot t_p = -\frac{q(t)}{A\epsilon_0}\left(g - z(t) + \frac{t_p}{\epsilon_r}\right) + \frac{\sigma}{\epsilon_0}\left(g - z(t)\right) \quad (2)$$

where $g$ is the maximum distance between the triboelectric pair, $z(t)$ is the displacement of the movable micro plate, and $t_p$ is the thickness of the polyimide layer. Further, the generated voltage is connected to the internal resistance $R$, which gives the expression of the current as

$$\dot{q}(t) = \frac{V(t)}{R} = -\frac{q(t)}{A\epsilon_0 R}\left(g - z(t) + \frac{t_p}{\epsilon_r}\right) + \frac{\sigma}{\epsilon_0 R}\left(g - z(t)\right) \quad (3)$$

Based on the displacement of the movable micro plate, two mechanical scenarios should be considered. The first happens when the displacement is smaller than the air gap ($z(t) < g$) and the governing equation of motion is given by

$$m\ddot{z}(t) = -c_m\dot{z}(t) - k_{eq}z(t) + F_e - ma(t) \quad (4)$$

Besides the forces from the equivalent stiffness $k_{eq}$, damping coefficient $c_m$, and the external acceleration $a(t)$, there is an electrostatic force on the micro plate from the effect of the capacitor given by

$$F_e = \frac{q^2(t)}{2\epsilon_0 A} \quad (5)$$

The second scenario happens when the displacement is beyond the initial air gap ($z(t) \geq g$), in which the impact force causes an additional stiffness $k_i$, another damping constant $c_i$, and the electrostatic force is not considered:

$$m\ddot{z}(t) = -c_i\dot{z}(t) - k_{eq}z(t) - k_i\left(z(t) - g\right) - ma(t) \quad (6)$$

We conduct the nondimensionalization by replacing with $\hat{z}(t) = z(t)/g$, $\hat{q}(t) = q(t)/(\sigma A)$, and $\hat{t} = t/T = t\sqrt{k_{eq}/m}$, to solve the electro-mechanical equations:

$$\frac{\partial^2\hat{z}}{\partial\hat{t}^2} = \begin{cases} -\frac{c_m T}{m}\frac{\partial\hat{z}}{\partial\hat{t}} - \hat{z}(T\hat{t}) + \frac{\sigma^2 AT^2}{2m\epsilon_0 g}\hat{q}^2(T\hat{t}) - \frac{T^2}{g}a(T\hat{t}), & \text{when } \hat{z}(t) < 1 \\ -\frac{c_i T}{m}\frac{\partial\hat{z}}{\partial\hat{t}} - \hat{z}(T\hat{t}) - \frac{k_i}{k_{eq}}\left(\hat{z}(T\hat{t}) - 1\right) - \frac{T^2}{g}a(T\hat{t}), & \text{when } \hat{z}(t) \geq 1 \end{cases} \quad (7)$$

$$\begin{aligned} \frac{\partial\hat{q}}{\partial\hat{t}} &= -\frac{Tg}{\epsilon_0 RA}\hat{q}\left(1 - \hat{z}(T\hat{t}) + \frac{t_p}{g\epsilon_r}\right) + \frac{Tg}{\epsilon_0 RA}\left(1 - \hat{z}(t)\right) \\ &= \frac{Tg}{\epsilon_0 RA}\left(1 - \hat{z}(T\hat{t})\right)\left(1 - \hat{q}\right) - \frac{Tt_p}{\epsilon_0\epsilon_r RA}\hat{q} \\ &= \alpha\left(\beta - \hat{z}(T\hat{t})\right)\left(1 - \hat{q}\right) - \gamma\hat{q} \end{aligned} \quad (8)$$

To verify our electro-mechanical model, we determined the generated voltages by applying different sinusoidal accelerating forces. Some of the model parameters (impact-related stiffness and damping, charge density $\sigma$, and resistance of TENG $R$) are identified from the experiments and listed in Table 2. Based on more detailed investigations [52], some specific parameters vary with different vibrational amplitudes of the TENG. Here, for simplicity, we assume them to

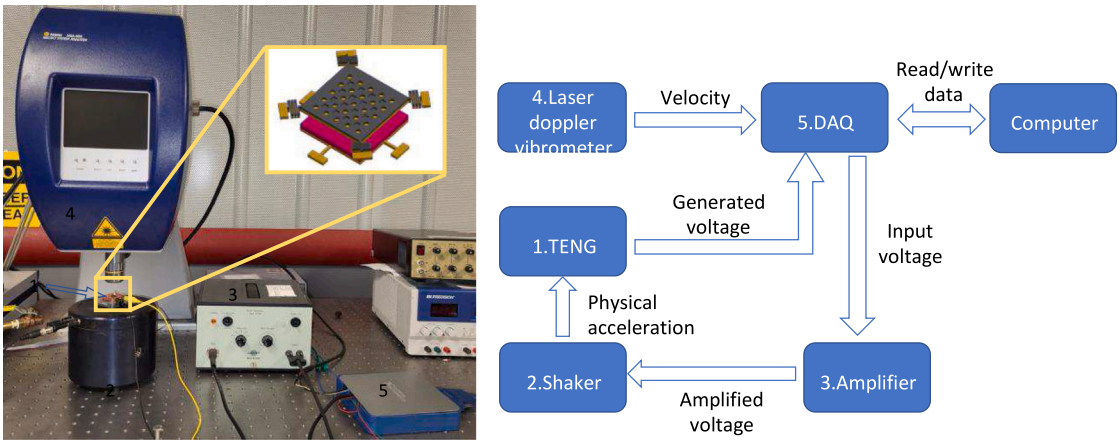


(a) (b)

**Fig. 3.** (a) Image of the experimental setup, and (b) schematic for the experimental setup where 1 is the fabricated MTEA, 2 is the shaker (B & K 4809), 3 is the amplifier (B & K 2706), 4 is the laser Doppler vibrometer (MSA-500), and 5 is the data acquisition system (USB 6366).

**Table 2**
Identified parameters of the TMEA from experimental results.

| Parameters | Symbol | Value |
|---|---|---|
| Mass of movable structure | $m$ | $9.32 \times 10^{-9}$ kg |
| Equivalent stiffness | $k_{eq}$ | 0.1803 N/m |
| Non-impact damping coefficient | $c_m$ | $3 \times 10^{-4}$ Ns/m |
| Impact stiffness | $k_i$ | $20 \times k_{eq}$ |
| Impact damping coefficient | $c_i$ | $3 \times c_m$ |
| Charge density | $\sigma$ | 15 μC/m$^2$ |
| Resistance of TENG | $R$ | $5G$ Ω |
| Vacuum permittivity | $\epsilon_0$ | $8.854 \times 10^{-12}$ F/m |
| Dielectric constant | $\epsilon_r$ | 3 |

be fixed values. Models using those fixed values produce simulations that adequately comply with experimental data. The results are fully discussed in Section 4.

## 4. Results and discussion

The experimental setup for the micro triboelectric accelerometer (MTEA) is shown in Fig. 3a and b. The micro triboelectric accelerometer (MTEA) is mounted on a portable vibration exciter, Bruel & Kjaer 4809, which is connected to a power amplifier, Bruel & Kjaer 2706. Those devices are controlled by a computer through a data acquisition system, NI USB-6366 which is used for sending data for the shaker and reading the MTEA output and the velocity from the vibrometer. The acceleration is acquired from numerical derivation of the measured velocity.

### 4.1. Sinusoidal vibrations testing

A laser Doppler vibrometer, Polytec MSA-500, is used to measure the velocities of the shaker (with the mass of the MTEA chip added) and to characterize the output accelerations resulting from the excitation of the shaker. The input voltages to keep the accelerations constant at different frequencies are recorded. The sinusoidal vibrations testing uses those input values and the output voltage from the MTEA is measured. For sinusoidal excitation, a 2–10 g acceleration input is applied to the MTEA in the range of 100 Hz–7 kHz. With the parameters identified in Table 2, our model efficiently predicted the linearity in the generated voltages in the frequency range between 700 Hz to 5 kHz, as the comparison with experimental data shows in Fig. 4a. The fundamental reason our model could not account for the responses outside that frequency range comes from some resonances of our MTEA (near and below 700 Hz) and resonances of the portable shaker (near and above 5 kHz). The discrepancy between the simulations and the experiments could be caused by varying resistances and charge densities at different vibrational amplitudes. The plot in Fig. 4b shows that the MTEA gives linear outputs against the accelerations for each frequency. Maximum slopes are identified near the natural frequency of our MTEA (around 700 Hz), which represent the greatest sensitivities when accelerations are measured. The sensitivity is maximized at 68.3 mV/g while the minimum sensitivity is 6.23 mV/g at 5 kHz. Besides acceleration-output linearity, the frequency responses of the MTEA in Fig. 4c have peaks near the natural frequency at different external accelerations. The root mean square (RMS) of the output voltage of the MTEA is shown in Fig. 4d against acceleration and frequency.

### 4.2. Shock pulses testing

To evaluate how fast or slow the micro triboelectric accelerometer (MTEA) responds, we use pulses of different heights and slopes as input voltages to the shaker. The data acquisition system synchronized the vibration accelerations (obtained from the laser Doppler vibrometer) and the generated voltages from the MTEA.

First, we input square signals of two different strengths (first: +1.5 V, second: +0.5 V) and long-enough duration into the shaker to activate positive and negative acceleration spikes. As in Fig. 5a, the two levels of generated voltages from the MTEA follow the strengths of the accelerating excitation very well. For first and second shock testing with pulse accelerations, the signal-to-noise ratios are calculated as 34.054 dB and 29.331 dB, respectively.

Next, we input trapezoidal signals of two different slopes (third: +3 V/s and −3 V/s, fourth: +3 V/s and −0.6 V/s) into the shaker to activate acceleration spikes of different strengths. As in Fig. 5b, the output voltages from the MTEA follow the levels of the accelerating excitation. Meanwhile, we observe detailed charging and discharging in generated voltage signals. Because the accelerations to TENG are much smaller than in the previous case, the charge generated from triboelectricity is much less. We assume the discharging starts almost at the same time as generating charges. When the generation of charges is weak, the discharging becomes more obvious. For third and fourth shock testing with pulse accelerations, the signal-to-noise ratios are calculated as 22.947 dB (+3 V/s) and 22.947 dB (−3 V/s), and 22.947 dB (+3 V/s) and 11.059 dB (−0.6 V/s), respectively. We conclude that when the external accelerations are below 0.5 m/s$^2$, our MTEA cannot respond well because of low signal to noise ratio.

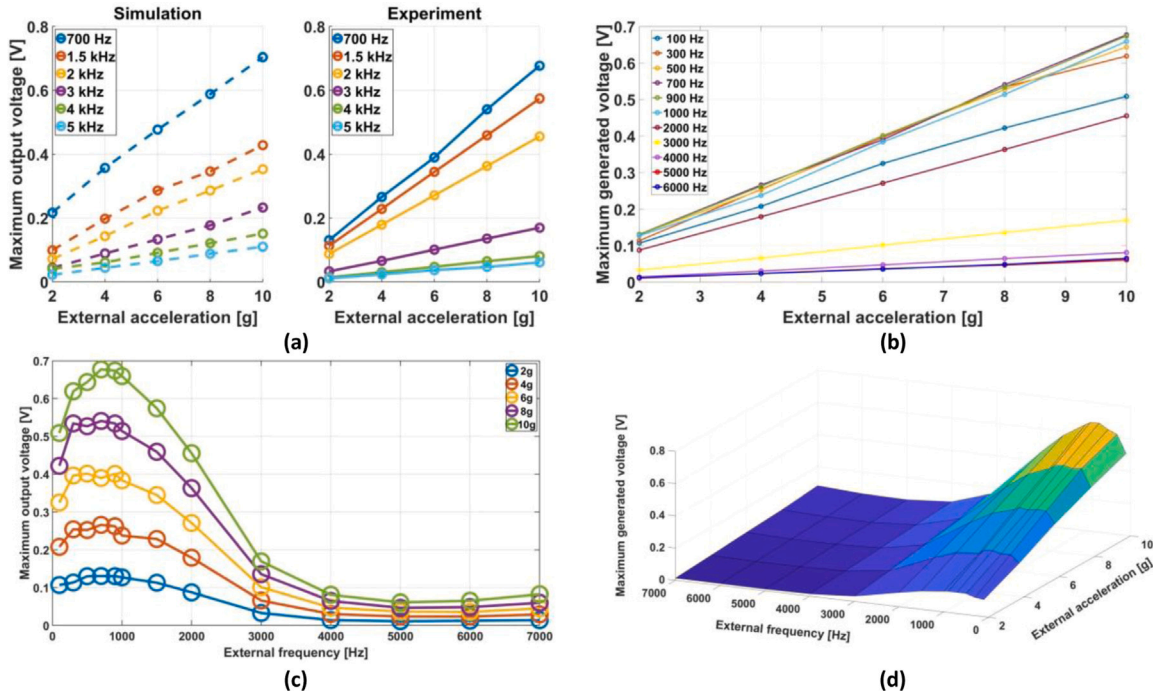


**Fig. 4.** Results of sinusoidal excitation where: (a) is the response comparison between simulation (left, dashed) and experiment (right, solid), (b) is the linear relationship between generated voltages and external accelerations with varying frequencies, (c) shows the peaks in the relationship between generated voltages and external frequencies with varying accelerations, and (d) shows complete RMS responses of the MTEA.

### 4.3. Cross-axis sensitivity

The MTEA's serpentine springs mostly allow out-of-plane (Z-axis) motion. The response of the MTEA for in-plane (X and Y axes) motions is tested by attaching a 3D-printed adapter to the shaker's table to mount the MTEA perpendicular to the table's surface in both axes. Then, the shaker is excited under different frequencies and the MTEA's output and acceleration are measured. The results for both axes sensitivity are shown in Fig. 6. In Fig. 6a, the sensitivity for excitation in $X$-axis is shown for 3 frequencies that fall in the test beginning, mid-range, and end region of applied frequencies tested in the previous section, the output was very small in comparison with the main axis excitation (Z-axis) and only 0.8–2.3 mV was recorded. A very close outcome was obtained by rotating the accelerometer 90 degrees to test $Y$-axis excitation with output falling in the range of 0.6 to 1.7 mV for 2–10 g excitation at the same frequencies. This output of $Y$-axis excitation is shown in Fig. 6b.

The accelerometer testing for the X and Y axes is important to check for the effect of disturbances on the designed system, with a harmonic disturbance, the system could be excited in higher-order mode shapes and give faulty measurements depending on how these modes cause the triboelectric pair of the MTEA to contact and separate.

The sensitivity for the accelerometer after X and Y axes excitation is shown in Fig. 6c. The measured sensitivity of these axes ranges from 0.016 mV/g to 0.1 mV/g which is negligible to the sensitivity from the Z-axis measurement that ranged from 6–70 mV/g. Also, the measurement of such low output has a very low signal-to-noise ratio compared to the output from $Z$-axis excitation. In this test, the main axis sensitivity was found to be 60–700 times higher than the sensitivity at the X and Y axes which is a considerable advantage for the MTEA. The high sensitivity in the normal direction and almost zero response in the other directions, shows an excellent potential of the MEMS-TENG to be engineered as a 3D accelerometer. Because of its small size, two other accelerometers with the same design can be positioned in perpendicular axes to make its 3D version. Its size will be orders of magnitude smaller than previous 3D TENG accelerometers [45] (the volume of our device should be around 0.00085% of the previous device's).

### 4.4. Accelerometer stability and long time performance

To test the accelerometer stability over long time, the device was tested two times separated by 6 months period for 2000 cycles. The results of this test for 3 different frequencies is shown in Fig. 7a–c. The device testing was conducted over the span of 8 months after it was released in a cleanroom and wire-bonded for testing. The linear relationship between acceleration and generated voltage with sinusoidal excitation is preserved with variation noticed in the peaks. The voltage variations at the natural frequency of the accelerometer (700 Hz) are higher than the variations far from resonance which happened because of the shift in the natural frequency for the system after being stored in air for about 7 months. The device has shown stability in its performance over time and had variations in the range of 2% to 37%.

### 4.5. Humidity effect on the accelerometer performance

Humidity is a major factor affecting MEMS devices performance. By conducting the test at two different times of the year (mid-summer and mid-winter), the effect of humidity on the performance of the accelerometer was noticed by variations in the results after repeating the same tests. The device was tested in atmospheric pressure at the room temperature. The test showed a shift in the natural frequency from 700 Hz to 1.1 kHz when the relative humidity changed from 40% to 15% as illustrated in Fig. 8a–b. The results has also shown drop in the generated voltage with lower relative humidity where the maximum voltage generated was 0.7 V at relative humidity of 40% and the generated voltage was 0.5 V at the relative humidity of 15%. The maximum output showed a variation of 30% around the peak frequency at 10 g. On the other hand, the variation away from the natural frequency at 5 kHz was the smallest as it ranged from 1 to 3% for accelerations 2–10 g.

### 4.6. Noise floor from Allan deviation theory

Allan deviation analysis has been widely applied to study the long-term performance of inertial MEMS sensors. Based on that, we turned

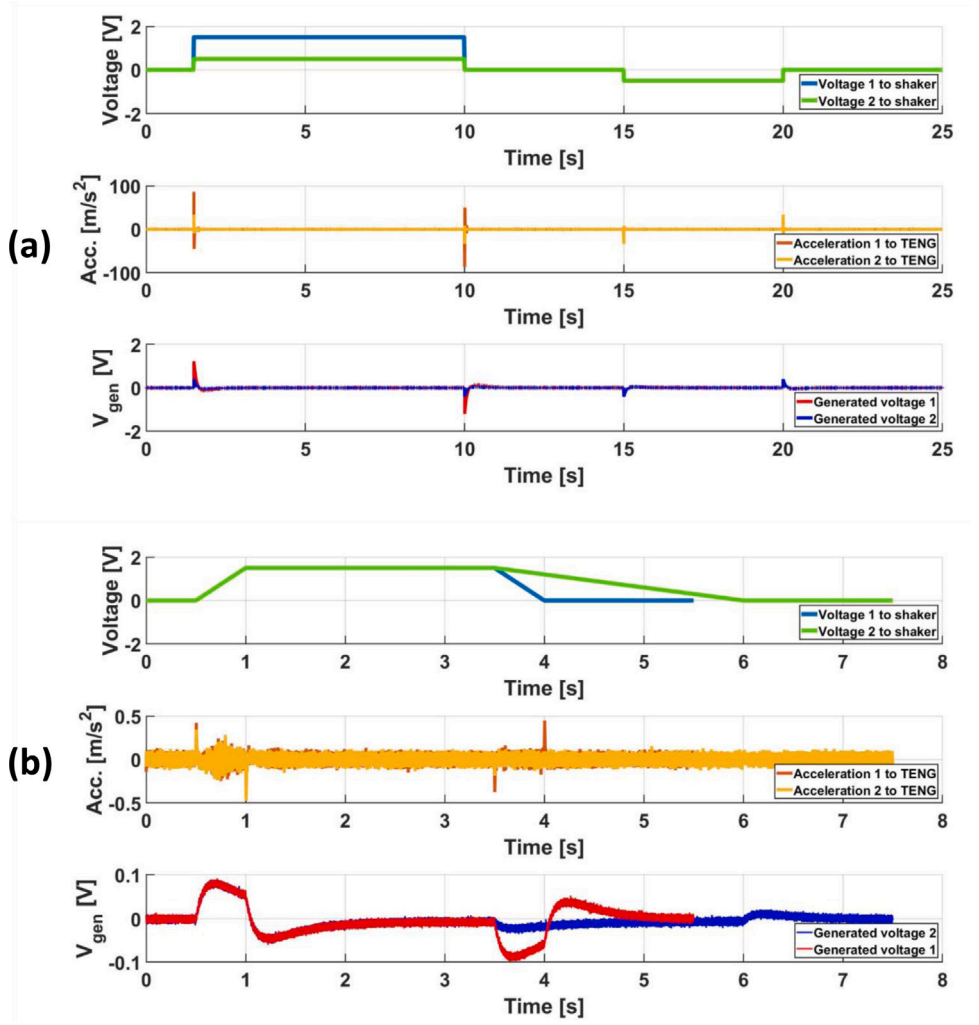


**Fig. 5.** (a) First and second shock testing with pulse accelerations. (b) Third and fourth shock testing with pulse accelerations.

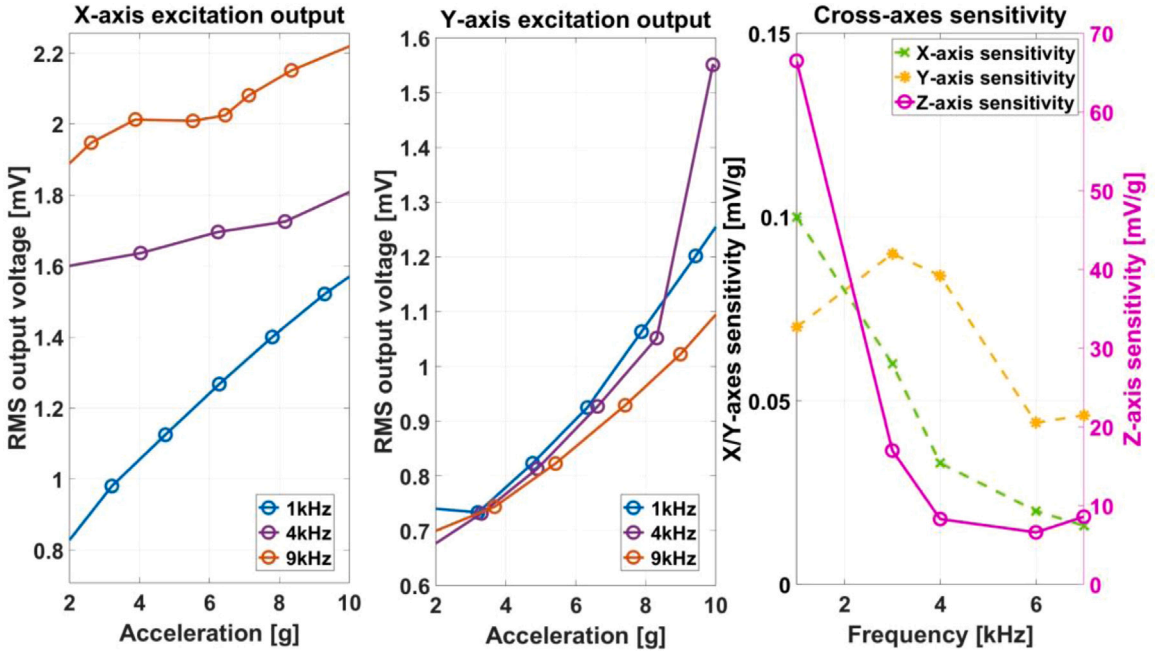


**Fig. 6.** RMS output voltages of TENG from: (a) *X*-axis excitation and (b) *Y*-axis excitation. (c) Sensitivity in X, Y, and Z axes.

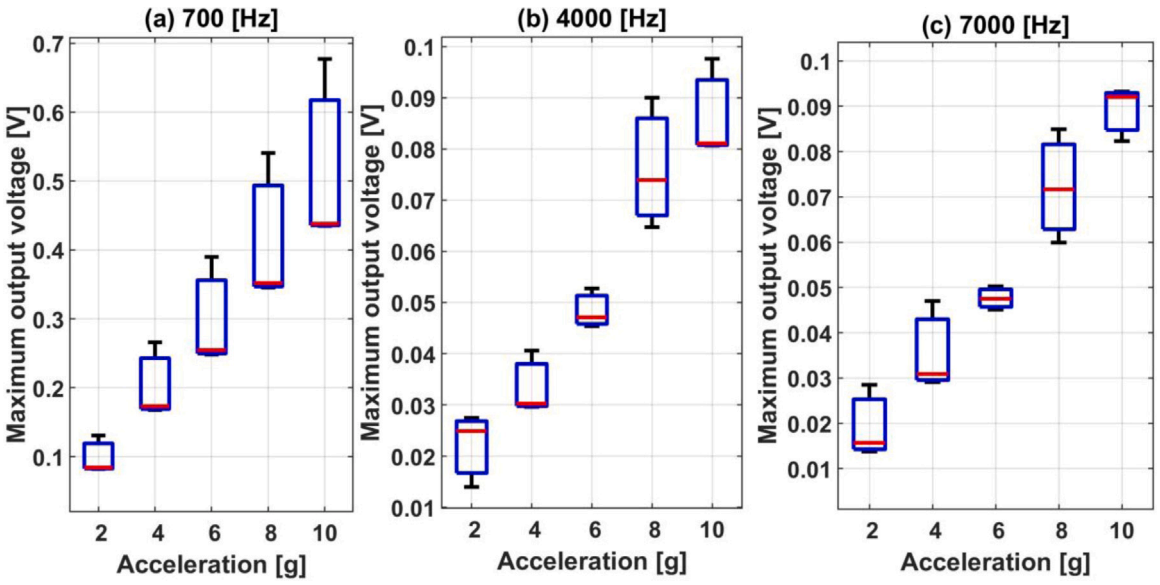


**Fig. 7.** Box-plots for 3 experiments done on the accelerometer to show long-time performance at external frequency of: (a) 700 Hz, (b) 4000 Hz and (c) 7000 Hz.

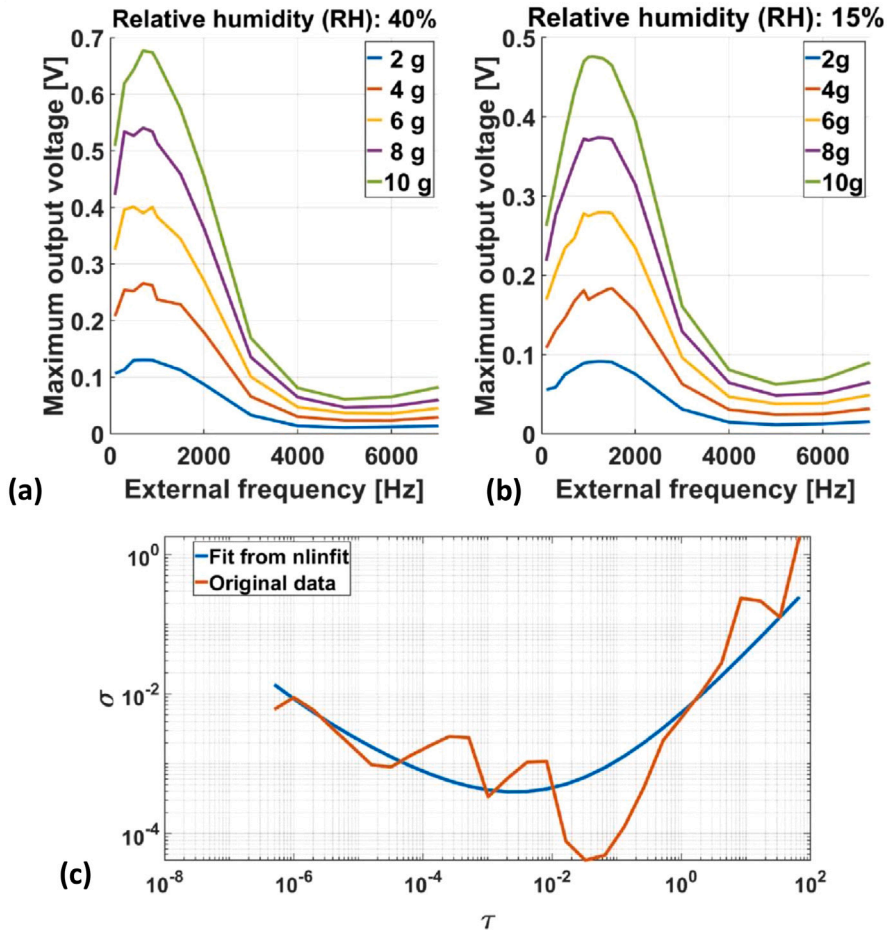


**Fig. 8.** (a) Frequency response of accelerometer at high RH (40%) and (b) frequency response of accelerometer at low RH (15%). (c) Tau-sigma curves from Allan deviation analysis.

**Table 3**
Coefficients determined from Allan deviation analysis.

| Coefficient | Relationship | Noise type | Parameters for MTEA |
|---|---|---|---|
| $A_{-2}$ | $Q = A_{-2}/\sqrt{3}$ | Quantization (Q) | $2.4319 \cdot 10^{-8}$~$2.6661 \cdot 10^{-7}$ [m/s] |
| $A_{-1}$ | $N = A_{-1}$ | Velocity random walk (N) | $7.9946 \cdot 10^{-5}$~$8.7645 \cdot 10^{-4}$ [m/s/$\sqrt{s}$] |
| $A_0$ | $B = A_0/0.664$ | Bias instability (B) | 4.1303~45.2810 [mg] |
| $A_1$ | $K = A_1 \cdot \sqrt{3}$ | Rate random walk (K) | 0.0439~0.4816 [m/s$^2$/$\sqrt{s}$] |
| $A_2$ | $R = A_2 \cdot \sqrt{2}$ | Rate ramp (R) | 0.0717~0.7859 [m/s$^3$] |

**Table 4**
Analog accelerometer product feature comparison.

| Parameter | ADXL326 (Analog Devices) | FXLN8372Q (NXP) | Our device |
|---|---|---|---|
| g-Range [g] | ±16 | 4~16 | ±10 |
| Sensitivity [mV/g] | 51~63 | 114.5 | 6.23~68.3 |
| Bias instability (B) [mg] | 0.42~1.06 | 6.55 | 4.13~45.28 |
| Velocity random walk (N) [m/s/$\sqrt{h}$] | 1.92~2.34 | 0.117~0.126 | 0.0048~0.053 |
| Cross-sensitivity | ±1% | ±4.2% | ±1% |

off the vibration shaker and recorded generated output voltages from the MTEA with the highest sampling rate of our data acquisition system, 2 MS/s. A sigma-tau logarithmic plot of the Allan deviation versus the cluster time is shown in Fig. 8c for the performance of the MTEA. Regression has been proven a powerful tool to extract Allan deviation parameters from experimental data [53]. With MATLAB, we use the nonlinear regression function, nlinfit.m, to fit the original data with the relationship in Eq. (9) and identify the coefficients in Table 3:

$$\sigma_{FIT}(\tau) = A_{-2}\tau^{-1} + A_{-1}\tau^{-0.5} + A_0\tau^0 + A_1\tau^{0.5} + A_2\tau^1 \quad (9)$$

To conclude assessment of the competitive performance of our device, we compare some critical parameters with those of two commercial analog accelerometers, as shown in Table 4. Regarding the g-range and bandwidth, our testable range is greatly restricted by the characteristics of the portable shaker and the power amplifier. But a comparable g-range and bandwidth of 100 Hz to 2 kHz (considering a 3 dB drop from the maximum generated voltage as the cutoff) are still secured. Our device shows a higher bias instability than the other two accelerometers, meaning a higher zero-g level offset is needed for an accurate measurement. The most negligible velocity random walk tells us our device is the best in long-time measurement with the slightest drift. The cross-sensitivity of our device is excellent. Together with the self-powered novelty of triboelectricity, our device has successfully implemented a TENG-based MEMS accelerometer in CMOS processes.

### 4.7. Discussion

A comparison of this work with different accelerometers in the recent literature is presented in Table 5. Among various self-powered accelerometers, our proposed accelerometer is demonstrated with competitively small device dimensions, wide measurable input accelerations, and high sensitivity. It is noticed that Teflon and PTFE are widely used in fabricating previous triboelectric accelerometers. However, the materials (Al-Polyimide) applied in our fabrication show excellent CMOS compatibility and are supported by MEMS standards whenever high-volume fabrication is desired, which Teflon [42] and PTFE [45,54] do not readily provide. Because of its natural oxide layer, Aluminum is more stable than copper [54] which changes with time and will affect triboelectric performance for a long time. Our selection of materials for the triboelectric effect also benefits from our previous research for meso-scale TENG [52,55] where the Al/PDMS pair shows great stability in voltage generation and the charges from triboelectricity can be hold for hours. In this paper, we employed another substrate material, Polyimide, as the insulator layer in this paper to make the materials more compatible with the standard MEMS fabrication technology. Our choice of material, design of micro-surfaces and standard micro-fabrication enabled us to achieve sensitivity per volume of 1897.22 $\frac{\text{mV}}{\text{g mm}^3}$, which is an order of magnitude higher than what has been reported before. In summary, both advantages in the sensing parameters and fabrication techniques strongly illustrate our proposed self-powered accelerometer as a novel and promising device with a very high performance.

## 5. Conclusion

In this paper, we presented a self-powered micro triboelectric accelerometer. The working principle is based on the contact-separation mode triboelectric generator with a triboelectric pair of aluminum and polyimide. The device has 2 × 2 mm$^2$ square layers with a thickness of 100 nm aluminum and 1 μm thick amorphous silicon and 2 μm gap. The device was made by CMOS-compatible processes in a clean room which allows for production scalability. The device produces linear output for input acceleration for 2–10 g with output going up to 0.7 V, and the output was maximum at the natural frequency of the top electrode at 700 Hz. The device testing for cross-axes sensitivity yielded very low outputs and, hence, the device is mostly sensitive to only normal excitation. The sensitivity ratio of normal to in-plane directions is 600 to 700.

## CRediT authorship contribution statement

**Mohammad Alzgool:** Micro-Fabrication, Methodology, Conceptualization, Formal analysis, Writing – original draft, Writing – review & editing. **Yu Tian:** Formal analysis, Validation, Simulations, Writing – original draft, Writing – review & editing. **Benyamin Davaji:** Methodology, Project administration, Writing – review & editing. **Shahrzad Towfighian:** Conceptualization, Funding acquisition, Methodology, Project administration, Resources, Writing – review & editing.

## Declaration of competing interest

The authors declare that they have no known competing financial interests or personal relationships that could have appeared to influence the work reported in this paper.

## Data availability

Data will be made available on request.

## Acknowledgments

The authors would like to acknowledge the financial support of the National Science Foundation (NSF), United States through Grant #1919608. This work was performed in part at the Cornell NanoScale Science and Technology Facility, a member of the National Nanotechnology Coordinated Infrastructure, which is supported by the National Science Foundation, United States (Grant NNCI-2025233).

**Table 5**
Performance comparison of the presented accelerometer with the state-of-the-art designs from literature.

| Type | Device dimensions [mm] | Input accelerations [g] | Operating frequency [Hz] | Max output voltage/volume [V/mm$^3$] | Sensitivity/ volume [mV/g/mm$^3$] | Self-powered |
|---|---|---|---|---|---|---|
| This work (triboelectric) | 2 × 2 × 0.009 | 0~10 | 300~1000 | 19.44 | 1897.22 | ✓ |
| Triboelectric [42] | 5 × 3 × 0.015 | 0~10 | 1150 | 1.56 | 191.11 | ✓ |
| Triboelectric [45] | Each axis: 80 × 18 × 18 | 1.33~4.08 | – | 0.0019 | 0.0011 | ✓ |
| Triboelectric [56] | (macro scale) | 0.11~0.13 | 2~10 | – | – | ✓ |
| Triboelectric [54] | 90 × 68 × 3 | 0.10~0.46 | 30 | 0.0033 | 0.081 | ✓ |
| Piezoelectric [57] | 9 × 9 × 0.4 | 0~10 | 7200 | 0.0043 | 0.046 | ✓ |
| Piezoelectric [58] | 6500 × 4 × 0.525 | 0~10 | 200 | 0.000012 | 0.0012 | ✓ |
| Electrostatic [59] | 5 × 5 × 0.06 | 0~0.25 | 730 | 0.11 | 240 | ✗ |
| Electrostatic [60] | 3 × 3 × 0.42 | 0~1 | 1300 | 0.28 | 264.55 | ✗ |

## References


[1] W.J. Fleming, New automotive sensors—A review, IEEE Sens. J. 8 (11) (2008) 1900–1921, http://dx.doi.org/10.1109/JSEN.2008.2006452.

[2] S. Finkbeiner, MEMS for automotive and consumer electronics, in: 2013 Proceedings of the European Solid-State Device Research Conference, ESSDERC, 2013, pp. 9–14, http://dx.doi.org/10.1109/ESSDERC.2013.6818809.

[3] H.H. Asada, H.-H. Jiang, P. Gibbs, Active noise cancellation using MEMS accelerometers for motion-tolerant wearable bio-sensors, in: The 26th Annual International Conference of the IEEE Engineering in Medicine and Biology Society, 1, IEEE, 2004, pp. 2157–2160.

[4] G. Lammel, The future of MEMS sensors in our connected world, in: 2015 28th IEEE International Conference on Micro Electro Mechanical Systems, MEMS, IEEE, 2015, pp. 61–64.

[5] L. Huang, H. Li, B. Yu, X. Gan, B. Wang, Y. Li, R. Zhu, Combination of smartphone MEMS sensors and environmental prior information for pedestrian indoor positioning, Sensors 20 (8) (2020) 2263.

[6] J. Gnap, J. Jagelčák, P. Marienka, M. Frančák, M. Kostrzewski, Application of MEMS sensors for evaluation of the dynamics for cargo securing on road vehicles, Sensors 21 (8) (2021) 2881.

[7] C. Yang, B. Zhang, D. Chen, L. Lin, Drop-shock dynamic analysis of MEMS/package system, in: 2010 IEEE 23rd International Conference on Micro Electro Mechanical Systems, MEMS, IEEE, 2010, pp. 520–523.

[8] L. Rong, Z. Jianzhong, L. Ming, H. Xiangfeng, A wearable acceleration sensor system for gait recognition, in: 2007 2nd IEEE Conference on Industrial Electronics and Applications, 2007, pp. 2654–2659, http://dx.doi.org/10.1109/ICIEA.2007.4318894.

[9] X. Yuan, S. Yu, Q. Dan, G. Wang, S. Liu, Fall detection analysis with wearable MEMS-based sensors, in: 2015 16th International Conference on Electronic Packaging Technology, ICEPT, IEEE, 2015, pp. 1184–1187.

[10] S. Shin, H. Wen, H.-K. Kwon, G.D. Vukasin, T.W. Kenny, F. Ayazi, A dual-axis resonant accelerometer based on electrostatic stiffness modulation in epi-seal process, in: 2019 IEEE SENSORS, 2019, pp. 1–4, http://dx.doi.org/10.1109/SENSORS43011.2019.8956601.

[11] A. Aydemir, Y. Terzioglu, T. Akin, A new design and a fabrication approach to realize a high performance three axes capacitive MEMS accelerometer, Sensors Actuators A 244 (2016) 324–333.

[12] H. Zhang, X. Wei, Y. Ding, Z. Jiang, J. Ren, A low noise capacitive MEMS accelerometer with anti-spring structure, Sensors Actuators A 296 (2019) 79–86.

[13] M. Daeichin, R.N. Miles, S. Towfighian, Large-stroke capacitive MEMS accelerometer without pull-in, IEEE Sens. J. 21 (3) (2021) 3097–3106, http://dx.doi.org/10.1109/JSEN.2020.3027270.

[14] A. Aydemir, Y. Terzioglu, T. Akin, A new design and a fabrication approach to realize a high performance three axes capacitive MEMS accelerometer, Sensors Actuators A 244 (2016) 324–333, http://dx.doi.org/10.1016/j.sna.2016.04.007, URL https://www.sciencedirect.com/science/article/pii/S0924424716301522.

[15] H. Zhang, X. Wei, Y. Ding, Z. Jiang, J. Ren, A low noise capacitive MEMS accelerometer with anti-spring structure, Sensors Actuators A 296 (2019) 79–86, http://dx.doi.org/10.1016/j.sna.2019.06.051, URL https://www.sciencedirect.com/science/article/pii/S0924424718321307.

[16] S. Tez, U. Aykutlu, M.M. Torunbalci, T. Akin, A bulk-micromachined three-axis capacitive MEMS accelerometer on a single die, J. Microelectromech. Syst. 24 (5) (2015) 1264–1274, http://dx.doi.org/10.1109/JMEMS.2015.2451079.

[17] M. Daeichin, M. Ozdogan, S. Towfighian, R. Miles, Dynamic response of a tunable MEMS accelerometer based on repulsive force, Sensors Actuators A 289 (2019) 34–43, http://dx.doi.org/10.1016/j.sna.2019.02.007, URL https://www.sciencedirect.com/science/article/pii/S0924424718321149.

[18] D. Kong, D. Jiang, Y. Zhao, Electromagnetic suspension acceleration measurement model and experimental analysis, Electronics 9 (2) (2020) http://dx.doi.org/10.3390/electronics9020226, URL https://www.mdpi.com/2079-9292/9/2/226.

[19] U. Krishnamoorthy, R. Olsson, G. Bogart, M. Baker, D. Carr, T. Swiler, P. Clews, In-plane MEMS-based nano-g accelerometer with sub-wavelength optical resonant sensor, Sensors Actuators A 145–146 (2008) 283–290, http://dx.doi.org/10.1016/j.sna.2008.03.017, URL https://www.sciencedirect.com/science/article/pii/S0924424708001672. Special Issue: Transducers/07 Eurosensors XXI, The 14th International Conference on Solid State Sensors, Actuators and Microsystems and the 21st European Conference on Solid-State Transducers.

[20] M. Ahmadian, K. Jafari, A graphene-based wide-band MEMS accelerometer sensor dependent on wavelength modulation, IEEE Sens. J. 19 (15) (2019) 6226–6232, http://dx.doi.org/10.1109/JSEN.2019.2908881.

[21] B. Yang, B. Wang, H. Yan, X. Gao, Design of a micromachined Z-axis tunneling magnetoresistive accelerometer with electrostatic force feedback, Micromachines 10 (2) (2019) http://dx.doi.org/10.3390/mi10020158, URL https://www.mdpi.com/2072-666X/10/2/158.

[22] J. Yick, B. Mukherjee, D. Ghosal, Wireless sensor network survey, Comput. Netw. 52 (12) (2008) 2292–2330, http://dx.doi.org/10.1016/j.comnet.2008.04.002, URL https://www.sciencedirect.com/science/article/pii/S1389128608001254.

[23] J. Kimionis, W. Su, J. Hester, J. Bito, X. He, T.-H. Lin, M.M. Tentzeris, Zero-power sensors for smart objects: Novel zero-power additively manufactured wireless sensor modules for IoT applications, IEEE Microw. Mag. 19 (6) (2018) 32–47, http://dx.doi.org/10.1109/MMM.2018.2844031.

[24] B.S. Cook, R. Vyas, S. Kim, T. Thai, T. Le, A. Traille, H. Aubert, M.M. Tentzeris, RFID-based sensors for zero-power autonomous wireless sensor networks, IEEE Sens. J. 14 (8) (2014) 2419–2431, http://dx.doi.org/10.1109/JSEN.2013.2297436.

[25] V. Pinrod, R. Ying, C. Ou, A. Ruyack, B. Davaji, A. Molnar, A. Lal, Zero power, tunable resonant microphone with nanowatt classifier for wake-up sensing, in: 2018 IEEE SENSORS, 2018, pp. 1–4, http://dx.doi.org/10.1109/ICSENS.2018.8589792.

[26] R.R. Reddy, K. Komeda, Y. Okamoto, E. Lebrasseur, A. Higo, Y. Mita, A zero-power sensing MEMS shock sensor with a latch-reset mechanism for multi-threshold events monitoring, Sensors Actuators A 295 (2019) 1–10, http://dx.doi.org/10.1016/j.sna.2019.05.036, URL https://www.sciencedirect.com/science/article/pii/S0924424719301098.

[27] V. Pinrod, L. Pancoast, B. Davaji, S. Lee, R. Ying, A. Molnar, A. Lal, Zero-power sensors with near-zero-power wakeup switches for reliable sensor platforms, in: 2017 IEEE 30th International Conference on Micro Electro Mechanical Systems, MEMS, 2017, pp. 1236–1239, http://dx.doi.org/10.1109/MEMSYS.2017.7863640.

[28] V. Pinrod, A. Ruyack, R. Ying, B. Davaji, A. Molnar, A. Lal, PZT lateral bimorph based sensor cuboid for near zero power sensor nodes, in: 2017 IEEE SENSORS, 2017, pp. 1–3, http://dx.doi.org/10.1109/ICSENS.2017.8234416.

[29] H. Okada, H. Nogami, T. Kobayashi, T. Masuda, T. Itoh, Development of ultra low power wireless sensor node with piezoelectric accelerometer for health monitoring, in: 2013 Transducers & Eurosensors XXVII: The 17th International Conference on Solid-State Sensors, Actuators and Microsystems (Transducers & Eurosensors XXVII), 2013, pp. 26–29, http://dx.doi.org/10.1109/Transducers.2013.6626692.

[30] S.S. Lee, R.M. White, Self-excited piezoelectric cantilever oscillators, Sensors Actuators A 52 (1) (1996) 41–45, http://dx.doi.org/10.1016/0924-4247(96)80123-3, URL https://www.sciencedirect.com/science/article/pii/0924424796801233. Proceedings of the 8th International Conference on Solid-State Sensors and Actuators Eurosensors IX.

[31] M.-h. Xu, H. Zhou, L.-h. Zhu, J.-n. Shen, Y.-b. Zeng, Y.-j. Feng, H. Guo, Design and fabrication of a D33-mode piezoelectric micro-accelerometer, Microsyst. Technol. 25 (12) (2019) 4465–4474.

[32] P. Verardi, F. Craciun, M. Dinescu, Characterization of PZT thin film transducers obtained by pulsed laser deposition, in: 1997 IEEE Ultrasonics Symposium Proceedings. an International Symposium (Cat. No.97CH36118), Vol. 1, 1997, pp. 569–572 vol.1, http://dx.doi.org/10.1109/ULTSYM.1997.663086.

[33] S.J. Roundy, Energy Scavenging for Wireless Sensor Nodes with a Focus on Vibration to Electricity Conversion (Ph.D. thesis), 2003, p. 287, URL http://proxy.binghamton.edu/login. Copyright - Database copyright ProQuest LLC; ProQuest does not claim copyright in the individual underlying works; Last updated - 2021-05-25.

[34] F.-R. Fan, Z.-Q. Tian, Z. Lin Wang, Flexible triboelectric generator, Nano Energy 1 (2) (2012) 328–334, http://dx.doi.org/10.1016/j.nanoen.2012.01.004, URL https://www.sciencedirect.com/science/article/pii/S2211285512000481.

[35] Y. Li, Z. Zhao, Y. Gao, S. Li, L. Zhou, J. Wang, Z.L. Wang, Low-cost, environmentally friendly, and high-performance triboelectric nanogenerator based on a common waste material, ACS Appl. Mater. Interfaces 13 (26) (2021) 30776–30784.

[36] W. Tang, C. Zhang, C.B. Han, Z.L. Wang, Enhancing output power of cylindrical triboelectric nanogenerators by segmentation design and multilayer integration, Adv. Funct. Mater. 24 (42) (2014) 6684–6690.

[37] X. Chen, X. Xie, Y. Liu, C. Zhao, M. Wen, Z. Wen, Advances in healthcare electronics enabled by triboelectric nanogenerators, Adv. Funct. Mater. 30 (43) (2020) 2004673.

[38] R. Hinchet, W. Seung, S.-W. Kim, Recent progress on flexible triboelectric nanogenerators for selfpowered electronics, ChemSusChem 8 (14) (2015) 2327–2344.

[39] H. Yang, Y. Pang, T. Bu, W. Liu, J. Luo, D. Jiang, C. Zhang, Z.L. Wang, Triboelectric micromotors actuated by ultralow frequency mechanical stimuli, Nature Commun. 10 (1) (2019) 1–7.

[40] Y. Pang, X. Zhu, C. Lee, S. Liu, Triboelectric nanogenerator as next-generation self-powered sensor for cooperative vehicle-infrastructure system, Nano Energy 97 (2022) 107219, http://dx.doi.org/10.1016/j.nanoen.2022.107219, URL https://www.sciencedirect.com/science/article/pii/S2211285522003007.

[41] X. Chen, Y. Wu, J. Shao, T. Jiang, A. Yu, L. Xu, Z.L. Wang, On-skin triboelectric nanogenerator and self-powered sensor with ultrathin thickness and high stretchability, Small 13 (47) (2017) 1702929, http://dx.doi.org/10.1002/smll.201702929, URL https://onlinelibrary.wiley.com/doi/abs/10.1002/smll.201702929. arXiv:https://onlinelibrary.wiley.com/doi/pdf/10.1002/smll.201702929.

[42] H.M.A. Hamid, Z. Çelik-Butler, A novel MEMS triboelectric energy harvester and sensor with a high vibrational operating frequency and wide bandwidth fabricated using UV-liga technique, Sensors Actuators A 313 (2020) 112175, http://dx.doi.org/10.1016/j.sna.2020.112175, URL https://www.sciencedirect.com/science/article/pii/S0924424720306178.

[43] H. Yu, X. He, W. Ding, Y. Hu, D. Yang, S. Lu, C. Wu, H. Zou, R. Liu, C. Lu, Z.L. Wang, A self-powered dynamic displacement monitoring system based on triboelectric accelerometer, Adv. Energy Mater. 7 (19) (2017) 1700565, http://dx.doi.org/10.1002/aenm.201700565, URL https://onlinelibrary.wiley.com/doi/abs/10.1002/aenm.201700565. arXiv:https://onlinelibrary.wiley.com/doi/pdf/10.1002/aenm.201700565.

[44] C. Liu, Y. Wang, N. Zhang, X. Yang, Z. Wang, L. Zhao, W. Yang, L. Dong, L. Che, G. Wang, X. Zhou, A self-powered and high sensitivity acceleration sensor with V-Q-a model based on triboelectric nanogenerators (TENGs), Nano Energy 67 (2020) 104228, http://dx.doi.org/10.1016/j.nanoen.2019.104228, URL https://www.sciencedirect.com/science/article/pii/S2211285519309358.

[45] Y.K. Pang, X.H. Li, M.X. Chen, C.B. Han, C. Zhang, Z.L. Wang, Triboelectric nanogenerators as a self-powered 3D acceleration sensor, ACS Appl. Mater. Interfaces 7 (34) (2015) 19076–19082, http://dx.doi.org/10.1021/acsami.5b04516, PMID: 26262509. arXiv:https://doi.org/10.1021/acsami.5b04516.

[46] C. Chen, Z. Wen, J. Shi, X. Jian, P. Li, J.T. Yeow, X. Sun, Micro triboelectric ultrasonic device for acoustic energy transfer and signal communication, Nature Commun. 11 (1) (2020) 1–9.

[47] S. Basrour, L. Robert, X-ray characterization of residual stresses in electroplated nickel used in LIGA technique, Mater. Sci. Eng. A 288 (2) (2000) 270–274.

[48] R. Lawes, Manufacturing costs for microsystems/MEMS using high aspect ratio microfabrication techniques, Microsyst. Technol. 13 (1) (2007) 85–95.

[49] H.-K. Chang, Y.-K. Kim, UV-LIGA process for high aspect ratio structure using stress barrier and C-shaped etch hole, Sensors Actuators A 84 (3) (2000) 342–350.

[50] G. Turban, M. Rapeaux, Dry etching of polyimide in O 2-CF 4 and O 2-SF 6 plasmas, J. Electrochem. Soc. 130 (11) (1983) 2231.

[51] S. Niu, S. Wang, L. Lin, Y. Liu, Y.S. Zhou, Y. Hu, Z.L. Wang, Theoretical study of contact-mode triboelectric nanogenerators as an effective power source, Energy Environ. Sci. 6 (12) (2013) 3576–3583.

[52] A. Ibrahim, A. Ramini, S. Towfighian, Experimental and theoretical investigation of an impact vibration harvester with triboelectric transduction, J. Sound Vib. 416 (2018) 111–124, http://dx.doi.org/10.1016/j.jsv.2017.11.036, URL https://www.sciencedirect.com/science/article/pii/S0022460X17308088.

[53] J. Jurado, C.M. Schubert Kabban, J. Raquet, A regression-based methodology to improve estimation of inertial sensor errors using allan variance data, Navigation 66 (1) (2019) 251–263.

[54] Y. Lin, Y. Qi, J. Wang, G. Liu, Z. Wang, J. Zhao, Y. Lv, Z. Zhang, N. Tian, M. Wang, et al., Self-powered and autonomous vibrational wake-up system based on triboelectric nanogenerators and MEMS switch, Sensors 22 (10) (2022) 3752.

[55] M. Mousavi, M. Alzgool, S. Towfighian, Autonomous shock sensing using bi-stable triboelectric generators and MEMS electrostatic levitation actuators, Smart Mater. Struct. 30 (6) (2021) 065019.

[56] X. Zhao, G. Wei, X. Li, Y. Qin, D. Xu, W. Tang, H. Yin, X. Wei, L. Jia, Self-powered triboelectric nano vibration accelerometer based wireless sensor system for railway state health monitoring, Nano Energy 34 (2017) 549–555, http://dx.doi.org/10.1016/j.nanoen.2017.02.036, URL https://www.sciencedirect.com/science/article/pii/S2211285517301143.

[57] Z.-H. Chen, C.-Y. Li, S.-Y. Chu, C.-C. Tsai, Y.-H. Wang, H.-Y. Kao, C.-L. Wei, Y.-H. Huang, P.-Y. Hsiao, Y.-H. Liu, The design of aluminum nitride-based lead-free piezoelectric MEMS accelerometer system, IEEE Trans. Electron Devices 67 (10) (2020) 4399–4404.

[58] Y.-C. Lee, C.-C. Tsai, C.-Y. Li, Y.-C. Liou, C.-S. Hong, S.-Y. Chu, Fabrication and function examination of PZT-based MEMS accelerometers, Ceram. Int. 47 (17) (2021) 24458–24465, http://dx.doi.org/10.1016/j.ceramint.2021.05.161, URL https://www.sciencedirect.com/science/article/pii/S0272884221015613.

[59] Y. Guo, Z. Ma, T. Zhang, X. Zheng, Z. Jin, A stiffness-tunable MEMS accelerometer, J. Micromech. Microeng. 31 (2) (2020) 025005.

[60] W. Li, X. Zhou, J. Wu, Y. Lin, Z. Wang, L. feng Che, A MEMS accelerometer with double-sided symmetrical folded-beams on single wafer, in: 2017 IEEE 12th International Conference on Nano/Micro Engineered and Molecular Systems, NEMS, IEEE, 2017, pp. 194–197.